

Multiwavelength evidence of the physical processes in radio jets

D.M. Worrall & M. Birkinshaw

Dept of Physics, University of Bristol, Tyndall Ave, Bristol BS8 1TL, UK
d.worrall@bristol.ac.uk, mark.birkinshaw@bris.ac.uk

Abstract. Over the last few years, high-quality X-ray imaging and spectroscopic data from *Chandra* and XMM-Newton have added greatly to the understanding of the physics of radio jets. Here we describe the current state of knowledge with an emphasis on the underlying physics used to interpret multiwavelength data in terms of physical parameters.

1 Introduction

Jets in active galaxies emit over a wide range of energies from the radio to the γ -ray. Synchrotron radiation and inverse-Compton scattering are the two main radiation processes, with their relative importance depending on observing frequency and location within the jet. The thermally-emitting medium into which the jets propagate plays a major role in the properties of the flow and the appearance of the jets.

In this chapter, we concentrate primarily on the interpretation of observations of resolved jet emission. Much new information about jets has been gained over the past few years. The high spatial resolution of *Chandra* has been key to the study of X-ray jets, and the large throughput of XMM-Newton has assisted studies of the X-ray-emitting environments. While historically the search for optical jet emission has been carried out using ground-based telescopes, a major problem has often been one of low contrast with light from the host galaxy. The sharp focus of the Hubble Space Telescope (HST) helps to overcome this difficulty, and the HST is playing a particularly important role in optical polarization studies. The recent opening of the Very Large Array (VLA) data archive has greatly assisted multiwavelength studies of radio jets. It, together with the Australian Telescope Compact Array (ATCA) in the southern hemisphere, allows multifrequency radio mapping at angular resolutions well matched to *Chandra* and XMM-Newton. The combination of data from the radio to the X-ray has been a key element in advancing our understanding of jets.

Active-galaxy jets provide an exciting laboratory where the interplay of relativistic effects, plasma physics, and radiation mechanisms can be seen. Our purpose in this chapter is to provide an introduction to the field and some pointers to recent research.

Published in Lect. Notes Phys (2006), 693, 39--76
Springer-Verlag Berlin Heidelberg.

Eq. 7 has been corrected in this version.

2 Radiative processes

The non-thermal mechanisms of synchrotron radiation and inverse Compton scattering are described extensively in several places, e.g., [14, 49, 81, 96, 111], and descriptions of thermal radiation can be found, e.g., in [81, 111, 114, 123]. In the following sections we give equations important in the interpretation of jet emission in useful forms that are normally independent of the system of units.

2.1 Synchrotron radiation

The rate of loss of energy of an electron (or positron) of energy E is given by

$$-dE/dt = 2\sigma_{\text{T}}c\gamma^2\beta^2u_{\text{B}}\sin^2\alpha \quad (1)$$

where σ_{T} is the Thomson cross section, c is the speed of light, γ is the Lorentz factor of the electron ($= E/m_e c^2$), β is the speed of the electron in units of c , u_{B} is the energy density in the magnetic field, and α is the pitch angle between the direction of motion and the magnetic field. Averaging over isotropic pitch angles, $P(\alpha)d\alpha = (1/2)\sin\alpha d\alpha$,

$$-dE/dt = (4/3)\sigma_{\text{T}}c\gamma^2\beta^2u_{\text{B}} \quad (2)$$

The radiative lifetime of the electrons is usually calculated as

$$\tau_{\text{rad}} = E/(-dE/dt) \quad (3)$$

which, for energy losses proportional to energy squared, as here, is the time for any given electron to lose half of its energy. High-energy electrons, responsible for high-energy radiation, lose their energy fastest.

The spectral distribution function of synchrotron radiation emitted by monoenergetic electrons of Lorentz factor γ is rather broad. It is usual to define the critical frequency,

$$\nu_c = (3/2)\gamma^2\nu_g \sin\alpha \quad (4)$$

where ν_g is the non-relativistic electron gyrofrequency, which is proportional to the magnetic field strength, B . Written in SI units, $\nu_g = eB/2\pi m_e \approx 30B$ GHz, where B is in units of Tesla. As a rough approximation, something close to ν_c can be used as the frequency of emission, but for the full distribution function it is convenient to define $X = \nu/\nu_c$, and then the spectral distribution function depends on frequency through

$$F(\nu, \nu_c) = X \int_X^\infty K_{5/3}(\zeta) d\zeta \quad (5)$$

where $K_{5/3}$ is the modified Bessel function of order $5/3$. The spectrum peaks at $0.29\nu_c$, as shown in Fig. 1. The synchrotron spectrum from a distribution

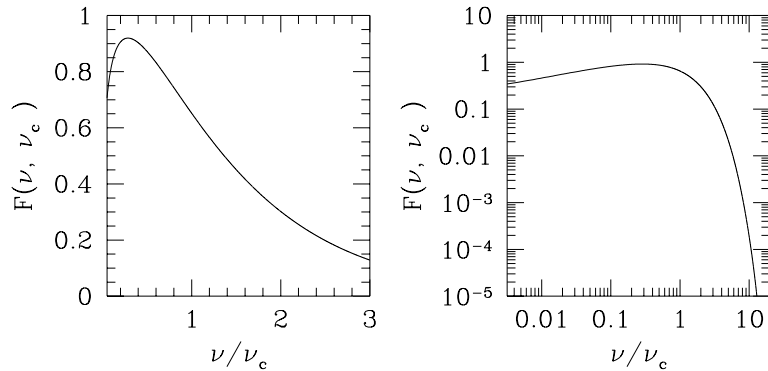


Fig. 1. The spectral distribution function of synchrotron radiation from a monoenergetic electron of Lorentz factor γ , where ν_c is defined in (4). The spectrum is plotted linearly on the left and logarithmically on the right

of electrons with some maximum Lorentz factor, γ_{\max} , will therefore fall exponentially at high frequencies. The gradual turn-down at low frequencies, $\propto \nu^{1/3}$, is not expected to be seen in practice. Instead, for a homogeneous emitting region the low-energy fall off will have a slope $\propto \nu^{2.5}$ due to the source having become optically thick and suffering from synchrotron self-absorption.

The luminosity per unit frequency for a number spectrum of electrons $N(\gamma)d\gamma$ is

$$L_\nu = 2\pi\sqrt{3} c m_e r_e \nu_g \sin \alpha \int F(\nu, \nu_c) N(\gamma) d\gamma \quad (6)$$

where r_e is the classical electron radius, and this form is valid in all systems of units. For a power-law number distribution of electrons $N(\gamma) d\gamma = \kappa \gamma^{-p} d\gamma$, an analytical result can be found for frequencies satisfying $\gamma_{\min}^2 \nu_g \ll \nu \ll \gamma_{\max}^2 \nu_g$

$$L_\nu = \kappa \nu^{-(p-1)/2} \nu_g^{(p+1)/2} \sin \alpha^{(p+1)/2} m_e c r_e \frac{3^{p/2} 2\pi}{p+1} \Gamma\left(\frac{p}{4} + \frac{19}{12}\right) \Gamma\left(\frac{p}{4} - \frac{1}{12}\right) \quad (7)$$

where Γ is the gamma function, and, again this form is valid in all systems of units. If the pitch angle distribution is isotropic, the term in $\sin \alpha$ may be replaced by $\sqrt{\pi} \Gamma[(p+5)/4] / 2\Gamma[(p+7)/4]$. The result for more complicated electron spectra must be computed numerically using (6).

It is usual to use the symbol α for the negative exponent of the power-law radiation spectrum ($L_\nu \propto \nu^{-\alpha}$), where $\alpha = (p-1)/2$. Particle acceleration by ultra-relativistic shocks, likely to be important in jets, produces $p \approx 2.2 - 2.3$ [1], and p will be steeper in regions where energy losses are important.

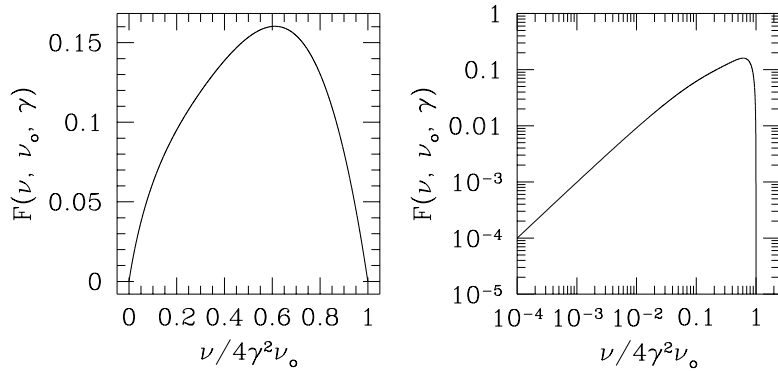


Fig. 2. The spectral distribution function of inverse Compton radiation from a monoenergetic electron of Lorentz factor γ in an isotropic radiation field of frequency ν_0 in the Thomson limit (8). The spectrum is plotted linearly on the left and logarithmically on the right

2.2 Inverse Compton scattering

Relativistic electrons lose energy by scattering photons to higher energy in a process analogous to synchrotron radiation, where virtual photons are replaced with real ones. Providing an electron of mass m_e and Lorentz factor γ is scattering a photon of low enough energy such that

$$\gamma h\nu_0 \ll m_e c^2 \quad (8)$$

the Thomson cross section, σ_T is applicable, and the rate of loss of energy of the electron in an isotropic radiation field of total energy density u_{rad} is

$$-dE/dt = (4/3)\sigma_T c \gamma^2 \beta^2 u_{\text{rad}} \quad (9)$$

where other symbols are as defined in Sect. 2.1. The radiative lifetime can be calculated using (3). Where electrons are losing energy both by synchrotron and inverse Compton emission, the ratio of total luminosity in the two emissions is simply $L_{\text{iC}}/L_{\text{syn}} = u_{\text{rad}}/u_{\text{B}}$.

An exact result [14] exists for the spectral distribution function for a monoenergetic electron of Lorentz factor γ scattering an isotropic radiation field of photons of frequency ν_0 up to frequency ν . It is convenient to define $X = \nu/4\gamma^2\nu_0$, where $(1/4\gamma^2) \leq X \leq 1$, and then the spectral distribution function is proportional to

$$F(\nu, \nu_0, \gamma) = Xf(X) = X(1 + X - 2X^2 + 2X \ln X) \quad (10)$$

This is plotted in Fig. 2. The luminosity per unit frequency for a number spectrum of electrons $N(\gamma)d\gamma$ and a spectral number per unit volume of photons $n(\nu_0)d\nu_0$ is

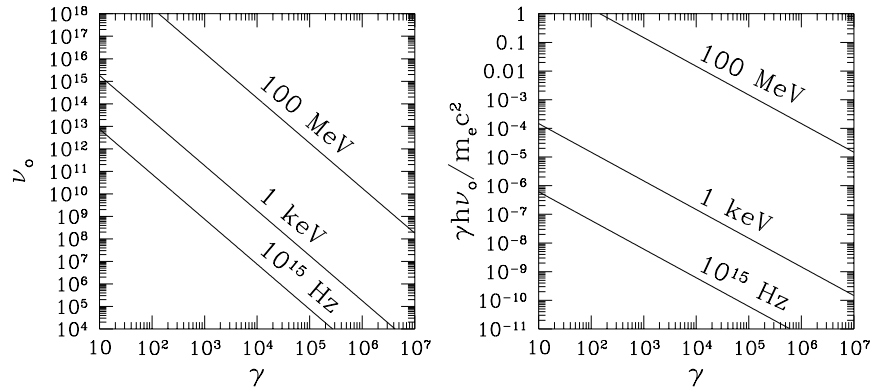


Fig. 3. The combinations of electron Lorentz factors and photon frequencies which will produce photons of typical optical, X-ray and γ -ray energies via inverse Compton scattering of an isotropic photon distribution in the Thomson limit is shown on the left. The Thomson limit only holds if $\gamma h \nu_o / m_e c^2 \ll 1$. The right-hand plot shows this is satisfied for optical and X-ray photons, but for γ -ray and higher energies the Klein-Nishina cross-section begins to become important

$$L_\nu = 3h c \sigma_T \int \int n(\nu_o) N(\gamma) F(\nu, \nu_o, \gamma) d\nu_o d\gamma \quad (11)$$

The relationship between the electron power-law index, p , and the spectral index of inverse Compton radiation, α , is the same as for synchrotron radiation. Since the mean value of X ,

$$\int X f(X) dX / \int f(X) dX = 1/3 \quad (12)$$

the mean frequency of photons scattered in an isotropic radiation field is given by

$$\nu = (4/3)\gamma^2\nu_o \quad (13)$$

Fig. 3 plots combinations of γ and ν_o that will produce optical, X-ray, and γ -ray photons according to (13), and shows that in most situations (8) is applicable. As (8) becomes violated, the Klein-Nishina cross section must be used in place of σ_T , as in these situations the electron begins to lose a significant fraction of its energy in a single scattering, e.g., [14].

The photon fields available to the electrons in jets are the synchrotron radiation they have produced, in which case the emission is known as synchrotron self-Compton (SSC) radiation, the cosmic microwave background (CMB) which scales with redshift as $(1+z)^4$, and photons from the active-galaxy nucleus. In practice the photon fields are rarely expected to be

isotropic when the effects of the geometry and bulk speed of the jet plasma are taken into account.

2.3 Thermal radiation and energy loss

For hot X-ray emitting gas containing ions of charge Z_i , and where the cooling in line radiation is unimportant, the X-ray emissivity, \mathcal{E}_ν depends on temperature, T , and electron and ion number densities, n_e , n_i , as

$$\mathcal{E}_\nu = \frac{32\pi}{3} \left(\frac{2\pi}{3}\right)^{1/2} Z_i^2 g_{\text{ff}} n_i n_e m_e c^2 r_e^3 \left(\frac{m_e c^2}{kT}\right)^{1/2} e^{-h\nu/kT} \quad (14)$$

for all systems of units, where r_e is the classical electron radius. $g_{\text{ff}}(\nu, T, Z)$, the free-free Gaunt factor which accounts for quantum-mechanical effects, is of order unity and a weak function of frequency. An approximate form [111] in the case of most X-ray interest, $(kT/\text{eV}) > 13.6Z_i^2$ and $Z_i \leq 2$, is

$$g_{\text{ff}} = \begin{cases} \left(\frac{3}{\pi} \frac{kT}{h\nu}\right)^{1/2} & h\nu > kT \\ \frac{\sqrt{3}}{\pi} \ln\left(\frac{4}{\zeta} \frac{kT}{h\nu}\right) & h\nu < kT \end{cases} \quad (15)$$

where the constant $\zeta = 1.781$. For heavier ions more complicated forms must be used, and since the heavier ions contribute disproportionately to the X-ray output (because of the Z_i^2 factor), the calculation of the correct Gaunt factor becomes a computational issue.

In SI units, (14) becomes

$$\mathcal{E}_\nu = 6.8 \times 10^{-51} Z_i^2 T^{-1/2} (n_e/\text{m}^{-3}) (n_i/\text{m}^{-3}) g_{\text{ff}} e^{-h\nu/kT} \text{ W m}^{-3} \text{ Hz}^{-1} \quad (16)$$

At temperatures below ~ 2 keV, line radiation cannot be ignored, and the plasma models incorporated into X-ray spectral-fitting programs such as XSPEC [4] can be used to find \mathcal{E}_ν . Examples for plasma of $kT = 0.5$ keV and 5.0 keV are shown in Fig. 4. It is common to define the rate of loss of energy per unit volume per unit frequency per $n_p n_e$ as $\Lambda(\nu)$, where n_p is the proton number density. In XSPEC, $\Lambda(\nu)$ is normalized by $(1+z)^2 \int n_p n_e dV / 4\pi D_L^2$ in fitting to data, where V is volume and D_L is luminosity distance. This allows n_p to be determined assuming some geometry for the source, as illustrated in Sect. 4.

The total energy-loss rate per unit mass is given by

$$\epsilon = \frac{X \int \mathcal{E}_\nu d\nu}{m_{\text{H}} n_p} \quad (17)$$

where X is the mass fraction in hydrogen, which is 0.74 for normal cosmic (i.e., solar) abundances.

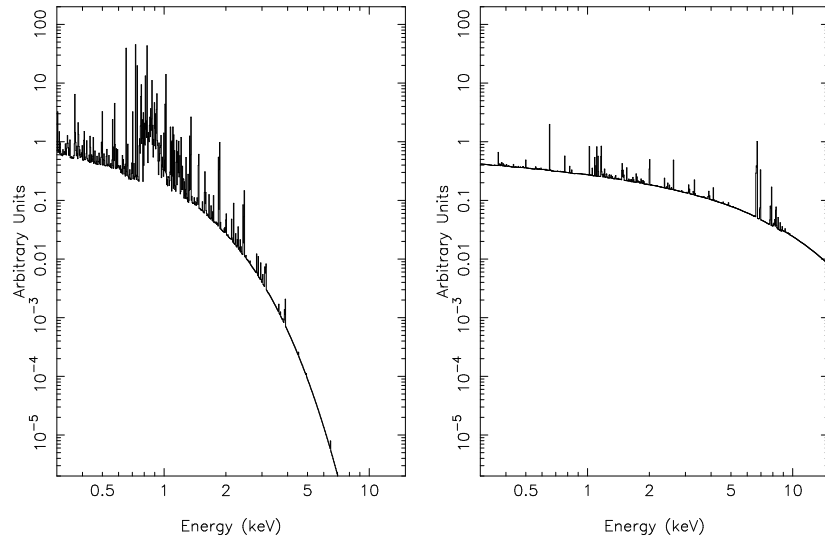


Fig. 4. Emissivity distributions of gas of $kT = 0.5$ keV (left) and $kT = 5$ keV (right) with normal cosmic abundances from the APEC model in XSPEC. The line emission, superimposed on the thermal bremsstrahlung continuum, is a more prominent channel for cooling in cool gas. The resolution of these model spectra is higher than that of current X-ray detectors

If the energy loss is sufficiently rapid, the radiating gas will fall towards the centre of the gravitational potential well as its pressure support fails. The rate of infall is therefore determined by whether the characteristic timescale for radiative energy loss is greater than or less than the timescale for energy input, perhaps from the dissipation of energy by the radio jet.

If the timescale for energy loss is defined by the logarithmic rate of change of temperature in the comoving fluid frame,

$$\tau_{\text{cool}} = - \left(\frac{D \ln T}{Dt} \right)^{-1} \quad (18)$$

where D/Dt is the convective derivative ($\partial/\partial t + \mathbf{v} \cdot \nabla$), which describes the rate of change in a frame moving at velocity \mathbf{v} with the gas, then the value of τ_{cool} can be obtained from the entropy equation

$$\frac{Ds}{Dt} = - \frac{\epsilon}{T} \quad (19)$$

where $s(T, P)$ is the entropy per unit mass of the gas and P is the pressure. For isobaric ($P = \text{constant}$) losses in a monatomic gas,

$$\tau_{\text{cool}} = \frac{5}{2} \frac{kT}{\epsilon \mu m_{\text{H}}} \quad (20)$$

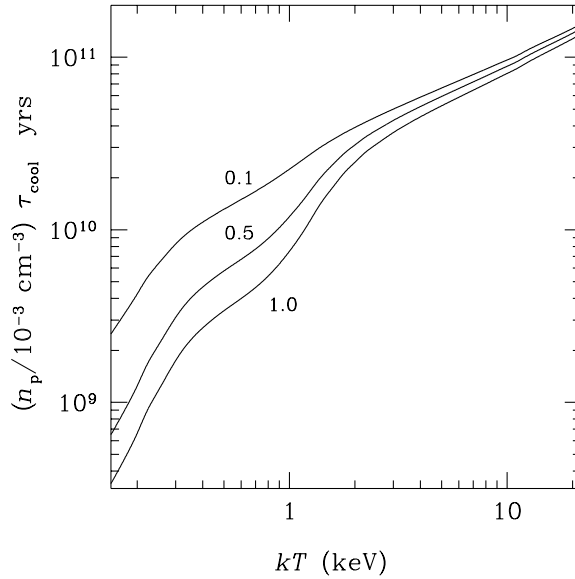


Fig. 5. Curves of $\tau_{\text{cool}}n_p$ (with n_p in units of 10^3 m^{-3} or 10^{-3} cm^{-3}) as a function of kT for three metal abundances with respect to solar: 0.1, 0.5, 1.0

Curves of $\tau_{\text{cool}}n_p$ as a function of kT , calculated using the APEC plasma model in XSPEC, are shown in Fig. 5. At high temperatures, $\tau_{\text{cool}} \propto T^{1/2}$, but at $T \leq 2$ keV line emission from common metal species in the gas becomes important, and so ϵ and τ_{cool} become strong functions of kT . The offset between the curves at large kT arises from the increased density of highly-charged ions in the radiating plasma as the metal abundance increases.

3 Effects of bulk relativistic motion

The first evidence for bulk relativistic motion in jets was on pc scales. In the early 1970s, the technique of Very Long Baseline Interferometry (VLBI) became established, and the first detections of apparent superluminal motion of small-scale radio components were being made (see [97] for a short review). After some years of debate, it became widely accepted that the true explanation of the effect was as proposed earlier, [107], and that the apparently superluminal velocities resulted from components moving towards the observer at bulk relativistic speeds.

From a consideration of light travel time, it is straightforward to show that a source moving with a relativistic speed βc , bulk Lorentz factor $\Gamma (= 1/\sqrt{1-\beta^2})$, at angle θ towards the observer, has an apparent transverse velocity of

$$v_{\text{app}} = \beta c \sin \theta / (1 - \beta \cos \theta) \quad (21)$$

which takes on a maximum value of $\Gamma\beta c$ when $\sin \theta = 1/\Gamma$. Hence large β ($> 1/\sqrt{2}$) and small θ can easily result in $v_{\text{app}} > c$.

The bulk relativistic Doppler factor is defined as

$$\delta = 1/\Gamma(1 - \beta \cos \theta) \quad (22)$$

and takes on a large value for large β , small θ . For a spherical blob of emission, the apparent spectral luminosity, L_ν , is increased by $\delta^{3+\alpha}$, where α is the spectral index (Sect. 2.1), although in most steady jets $\delta^{2+\alpha}$ is more appropriate [103, 116].

A variable source will show intensity changes on timescales shorter by δ than the true value, and beaming effects can have a dramatic effect on model parameters. For example, it was shown that the predicted X-ray flux density from SSC in a compact, spherical, variable radio source must be reduced by a factor of $\delta^{2(3\alpha+5)}$ if variability is used to measure the size, and the observed self-absorption turn-over frequency is used to estimate the magnetic-field strength [85, 86].

Relativistic beaming has a major effect on a jet's appearance, and by the 1980s the first models to unify classes of active galaxies through jet orientation were proposed, e.g., [94, 116], and subsequently further developed to account for multiwavelength properties, e.g., [6, 115, 130]. It is common to assume that a radio source has two oppositely-directed jets that are intrinsically the same, although there is doubt that this need be the case either from jet-production considerations or asymmetries in the environment through which the jets propagate. Under the assumption of intrinsic similarity, the brightness ratio between the approaching and receding jets is given by

$$R_J = \left(\frac{1 - \beta \cos \theta}{1 + \beta \cos \theta} \right)^{-(\alpha+2)} \quad (23)$$

This constraint on β and θ is often used in conjunction with a constraint on v_{app} to estimate separately the jet speed and the angle to the line of sight, e.g., [68, 147]. The core dominance, R_{cd} , defined as the flux density of beamed emission divided by that of unbeamed extended emission, is also commonly used as an indicator of the angle of a source to the line of sight. When applied to a twin-jet source, e.g., [94],

$$R_{\text{cd}} = \frac{R_{\text{cd}(\cos \theta=0)}}{2} \left[(1 - \beta \cos \theta)^{-(\alpha+2)} + (1 + \beta \cos \theta)^{-(\alpha-2)} \right] \quad (24)$$

Bulk relativistic motion towards the observer has an important effect on inverse-Compton scattering in the case of an external photon field (i.e., not SSC) [34]. In its rest frame an electron now sees a directionally enhanced

radiation field and the rate of scatterings increases. If the photon field is isotropic in the observer's frame (such as the CMB), the increase in scattering rate is by a factor of δ . Since lower-energy electrons (of which there are more) are needed to scatter photons of a given rest-frame frequency to the observed frequency, there is a further enhancement by δ^α . This means that the observed luminosity at a given frequency from inverse-Compton scattering of the CMB will be increased relative to the synchrotron luminosity by $\delta^{1+\alpha}$, assuming that the magnetic field and electron spectrum are held constant. Although this in itself is not a large factor compared with $\sim \delta^{2+\alpha}$ (see above) that arises from any radiation mechanism and applies both to the synchrotron and inverse-Compton emission, it can be sufficient to raise the ratio of X-ray to radio emission enough to fit observations of quasar jets (Sect. 6.3). For a source radiating at minimum energy (Sect. 6.1), while the X-ray emission from inverse-Compton scattering of CMB photons is increased, the X-ray emission from SSC is reduced. To increase this ratio via the SSC mechanism requires taking the source out of minimum energy through adding relativistic electrons. A beamed source has intrinsically lower total energy content, and, despite the higher jet speed increasing the kinetic energy, it may be in a condition of minimum total (radiative and kinetic) power [47].

4 The external medium

Often the bulk of the X-ray emission from an active galaxy is not jet related, but rather arises from the hot interstellar, intergalactic, or intracluster medium around the jet. If we assume that this gas is almost at rest in the local gravitational potential well, with little transfer of energy or matter to or from it, then it will be in a state close to hydrostatic equilibrium.

Under these circumstances, the gas will take up a density and temperature profile which depend on the distribution of mass and the thermal history of the gas. The principal governing equation is that of hydrostatic equilibrium, with

$$\nabla P = -\rho \nabla \Phi \quad (25)$$

where Φ is the gravitational potential and ρ is the total mass density of the gas. We may assume that the gas has the ideal gas equation of state

$$P = \frac{\rho k T}{\mu m_{\text{H}}} = \frac{n_{\text{p}} k T}{X \mu} \quad (26)$$

to relate P and ρ , where μ is the mass per particle in units of m_{H} , given by

$$\mu = \left(2X + \frac{3}{4}Y + \frac{1}{2}Z \right)^{-1} = 0.60 \quad (27)$$

for a gas with solar abundances ($X = 0.74$, $Y = 0.25$, $Z = 0.01$).

If the mass distribution is spherically symmetrical, then

$$\frac{d\Phi}{dr} = \frac{G M_{\text{tot}}(r)}{r^2} \quad (28)$$

where $M_{\text{tot}}(r)$ is the total mass within radius r , and so the mass density and temperature profiles of the gas are related to the distribution of total mass by

$$G M_{\text{tot}}(r) = -\frac{kTr}{\mu m_{\text{p}}} \left(\frac{d \ln \rho}{d \ln r} + \frac{d \ln T}{d \ln r} \right) \quad (29)$$

A consistent solution of this equation is obtained by assuming that the gas is isothermal and that the mass distribution follows

$$M_{\text{tot}}(r) = 2 M_{\text{c}} \frac{r^3}{r_{\text{c}}(r^2 + r_{\text{c}}^2)} \quad (30)$$

where r_{c} , the core radius, defines the characteristic scale of the mass distribution and M_{c} is the mass within r_{c} . The density of the gas then follows the so-called isothermal β model [25]

$$\rho = \rho_0 \left(1 + \frac{r^2}{r_{\text{c}}^2} \right)^{-\frac{3}{2}\beta} \quad (31)$$

where β is a constant which determines the shape of the gas distribution, and depends on the ratio of a characteristic gravitational potential to the thermal energy per unit mass in the gas

$$\beta = \frac{2}{3} \frac{\mu m_{\text{H}}}{kT} \frac{GM_{\text{c}}}{r_{\text{c}}} \quad (32)$$

The alternative derivation of (31) given by [25] brings out the interpretation of β in terms of the relative scale heights or, equivalently, the ratio of energy per unit mass in gas and dark matter. ρ_0 , r_{c} , and β in (31) are often fitted to provide convenient measures of the gas distribution's mass, scale and shape without considering the detailed properties of the underlying mass distribution (30).

It should be noted that the physical consistency of this much-used model for the gas distribution depends on radial symmetry (a simple distortion into an ellipsoidal model for the gas density ρ would imply a mass distribution which is not necessarily positive everywhere), and on gas at different heights in the atmosphere having come to the same temperature without having necessarily followed the same thermal history. This is problematic given the various origins of gas — some will have fallen into the cluster, some will have been ejected from stars, and some may have been moved by the jet. The solution (31) is not unique in the sense that gas with a different thermal history might follow a significantly different density distribution. Thus, for

example, if the gas has the same specific entropy at all heights, and so is marginally convectively unstable, with

$$P \propto \rho^\gamma \quad (33)$$

with γ being the usual specific heat ratio (5/3 for a monatomic gas), the mass distribution (30) would lead to a gas density distribution

$$\rho^{\gamma-1} = \rho_0^{\gamma-1} \left(1 - \beta_A \ln \left(1 + \frac{r^2}{r_c^2} \right) \right) \quad (34)$$

where β_A is a structure constant with a similar meaning to β , and the relation only applies within the radius at which $\rho \rightarrow 0$.

A similar procedure for an NFW mass profile [92] and an isothermal gas leads to a density distribution

$$\rho = \rho_s 2^{-\alpha} \left(1 + \frac{r}{r_s} \right)^{\alpha r_s / r} \quad (35)$$

where the new structure constant is

$$\alpha = \frac{1}{\ln 2 - \frac{1}{2}} \frac{\mu m_H}{kT} \frac{GM_s}{r_s} \quad (36)$$

(r_s is the scale of the NFW model and M_s is the mass within radius r_s). It can be seen that in this solution $\rho \rightarrow \infty$ as $r \rightarrow 0$, since the NFW density profile has a cusp at $r = 0$.

The total masses for either the NFW profile or (30) diverge as $r \rightarrow \infty$, so both profiles must be truncated at some radius, such as r_{200} , the radius at which the mean enclosed mass density is $200\times$ the critical density of the Universe, ρ_{crit} at redshift z . Care should be taken in using the solutions for ρ to ensure that the fraction of mass in gas does not exceed the cosmological bound ($\sim 17\%$).

The run of density and temperature in the atmosphere around a jet are measured from the X-ray image and spectrum, where a density model for the gas of the form of (31) or (35) is fitted to the X-ray surface brightness. The X-ray surface brightness at frequency ν at a point offset by r in *projected* distance from the centre of a spherical gas distribution is (in energy per unit time per unit solid angle per unit frequency)

$$\Sigma_\nu(r) d\Omega = (1+z) \frac{\int n_e n_p A_\nu(T) dV}{4\pi D_L^2} \quad (37)$$

where A_ν is the emissivity of the gas at frequency ν , and D_L is the luminosity distance of the gas. The $(1+z)$ factor takes account of the redshifting of time and frequency in the definition of Σ_ν . The volume element in the integral is

$$dV = dl D_A^2 d\Omega \quad (38)$$

where dl is an element of distance along the line of sight, D_A is the angular diameter distance, and $d\Omega$ is the element of solid angle, so that the surface brightness becomes

$$\Sigma_\nu(r) = \frac{\int n_e n_p A_\nu(T) dl}{4\pi(1+z)^3} \quad (39)$$

For an isothermal gas with a β -model density distribution

$$\Sigma_\nu(r) = \frac{A_\nu(T) n_{e0} n_{p0}}{4\pi(1+z)^3} \int \left(1 + \frac{r^2 + l^2}{r_c^2}\right)^{-3\beta} dl \quad (40)$$

where the integral is taken along the line of sight with limits of $\pm\infty$ or to some cut-off radius. In the former case the integral is simple, and the X-ray surface brightness can be written [11]

$$\Sigma_\nu(r) = \frac{A_\nu(T) n_{e0} n_{p0} r_c}{4\pi(1+z)^3} \left(1 + \frac{r^2}{r_c^2}\right)^{\frac{1}{2}-3\beta} \sqrt{\pi} \frac{\Gamma(3\beta - \frac{1}{2})}{\Gamma(3\beta)} \quad (41)$$

It is also useful to write down the observed flux density, S_ν , of a gas distribution out to angle θ from the centre, since this is the quantity generally fitted in X-ray spectral analyses. This is

$$S_\nu(\theta) = \int_0^\theta 2\pi\theta d\theta \Sigma_\nu(r) \quad (42)$$

$$= \frac{A_\nu(T) n_{e0} n_{p0} \theta_c^3 D_A}{(1+z)^3} \frac{\sqrt{\pi}}{4} \frac{\Gamma(3\beta - \frac{3}{2})}{\Gamma(3\beta)} \left(1 - \left(1 + \frac{\theta^2}{\theta_c^2}\right)^{\frac{3}{2}-3\beta}\right) \quad (43)$$

where θ_c is the angular equivalent of the core radius r_c . Now, **XSPEC** (Sect. 2.3) calculates a normalization, \mathcal{N} , for any thermal gas model, where

$$\mathcal{N} = \frac{\int n_e n_p dV}{4\pi D_A^2 (1+z)^2} \equiv \frac{(1+z) S_\nu}{A_\nu} \quad (44)$$

and this is related to the parameters of the isothermal β model by

$$\mathcal{N} = \frac{n_{e0} n_{p0} \theta_c^3 D_L}{(1+z)^4} \frac{\sqrt{\pi}}{4} \frac{\Gamma(3\beta - \frac{3}{2})}{\Gamma(3\beta)} \left(1 - \left(1 + \frac{\theta^2}{\theta_c^2}\right)^{\frac{3}{2}-3\beta}\right) \quad (45)$$

The fitting process in **XSPEC** takes account of the form of A_ν and the conversion from energy units (S_ν) to the count rate in energy bins used by X-ray detectors.

This expression shows how to use the normalization \mathcal{N} found by **XSPEC**, or some other code, from the X-ray spectrum within angular radius θ of the centre, and β and r_c as fitted from the radial profile of the X-ray emission, to measure the central electron and proton densities which are related by

$$\frac{n_e}{n_p} = \frac{1 + X}{2X} \sim 1.18 \quad (46)$$

The proton density found in this way, and the gas temperature measured from the spectrum, provide crucial information on the gas environments of radio jets and hence the external forces on the jet. The separation of X-rays from the non-thermal processes associated with the radio source and the thermal processes associated with the environment is therefore an important part of establishing the physics of a jet. This is particularly true for low power (FRI) jets, which are in direct contact with the external medium (Sec. 5.2), but is also important for establishing the balance of static and ram-pressures in powerful sources.

5 Simple radio-jet models

The FRI and FRII classifications, into which extragalactic radio sources were separated by [41], remain in wide usage today. Although based on radio morphology, [41] found a relatively sharp division in radio luminosity, with most sources of total 178-MHz luminosity below $2 \times 10^{25} \text{ W Hz}^{-1} \text{ sr}^{-1}$ being of FRI classification, and the others of FRII. Some dependence of the location of the FRI/FRII boundary on the optical magnitude of the host galaxy has also been found [95], suggesting the effects of environment or the mass of the originating black hole are important in determining the type of radio galaxy formed by an active nucleus. However, the primary cause of the structural differences is believed to be due to the speed of the primary jet fluid, with the beams producing FRII sources being supersonic with respect to the ambient medium, whereas FRI jets are seen as the result of turbulent transonic or subsonic flows. The following sub-sections describe the observational consequences.

5.1 High-power FRII jets

The standard model for the expansion of a powerful radio source powered by a jet which is supersonic with respect to the X-ray-emitting interstellar medium (ISM) is illustrated in Fig. 6. The jet terminates at the beam head (in a feature identified as the radio hotspot) where the jet fluid passes through a strong shock to inflate a cocoon of radio-emitting plasma. The energy and momentum fluxes in the flow are normally expected to be sufficient to drive a bow shock into the ambient medium ahead of the jet termination shock. In the rest frame of the bow shock, ambient gas is heated as it crosses the shock to fill a region surrounding the lobe of radio-emitting plasma. Observationally on kpc scales we see the radio emission from well-collimated jets feeding edge-brightened lobes. An example is shown in Fig. 7.

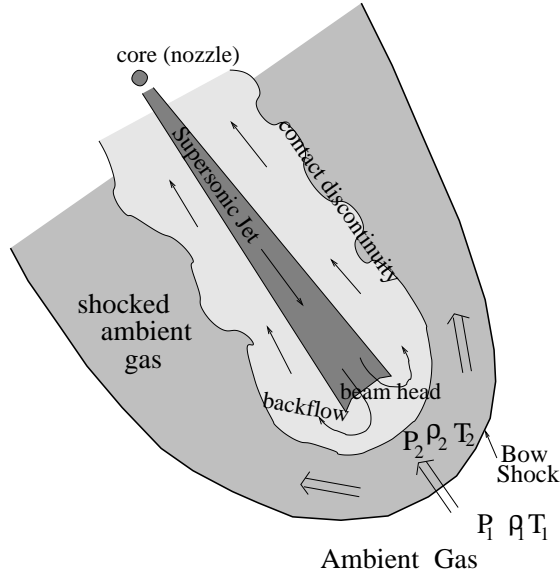


Fig. 6. In the standard model for powerful radio sources, a supersonic jet (dark grey) terminates at the beam head, producing a radio hotspot. Provided the shocked radio-emitting fluid forming the radio lobe (light grey) has enough internal energy or momentum density to drive a leading bow shock, ambient X-ray-emitting gas will be heated as it crosses the bow shock to fill the medium-grey region



Fig. 7. 8.4 GHz VLA A and B array radio image of an example high-power FRII source, the radio galaxy 3C 220.1. The resolution is 0.3×0.2 arcsec, and the image is from [145]. The angular length of the source is about 28 arcsec which, at the galaxy's redshift of $z = 0.61$, corresponds to 187 kpc ($H_o = 70 \text{ km s}^{-1} \text{ Mpc}^{-1}$, $\Omega_m = 0.3$, $\Omega_\Lambda = 0.7$)

The sound speed in gas of temperature T is

$$c_s = \sqrt{\frac{\gamma kT}{\mu m_H}} \quad (47)$$

where γ is the ratio of specific heats ($\gamma = 5/3$), k is the Boltzmann constant, m_H is the mass of the hydrogen atom, and $\mu m_H = 0.6m_H$ is the mass per particle. Under these conditions, $c_s \approx 516(kT/\text{keV})^{1/2} \text{ km s}^{-1} \approx 0.54(kT/\text{keV})^{1/2} \text{ kpc Myr}^{-1}$.

The Mach number of the speed of advance, v_{adv} , of the bow shock into the ambient medium is $\mathcal{M} = v_{\text{adv}}/c_s$, which in convenient units can be expressed as

$$\mathcal{M} \approx 580(v_{\text{adv}}/c)(kT/\text{keV})^{-1/2} \quad (48)$$

where c is the speed of light. The advance of the bow shock is likely to be slow with respect to the bulk speed of the jet. However, the jets need not have bulk relativistic motion (Sect. 3) for the general description of an FRII source to hold.

The state of the X-ray gas close to a radio galaxy with a leading bow shock should reflect the source dynamics, and in addition to the X-ray emission of the ambient medium (Sect. 4), we may also expect to see hotter shocked gas surrounding the radio lobe (Fig. 6). In a simple application of the Rankine-Hugoniot conditions for a strong shock [123], the pressure, density, and temperature, respectively, in the unshocked (subscript 1) and shocked (subscript 2) regions at the head of the bow shock are related by

$$P_2/P_1 = (5\mathcal{M}^2 - 1)/4 \quad (49)$$

$$\rho_2/\rho_1 = 4\mathcal{M}^2/(\mathcal{M}^2 + 3) \quad (50)$$

$$T_2/T_1 = (5\mathcal{M}^2 - 1)(\mathcal{M}^2 + 3)/16\mathcal{M}^2 \quad (51)$$

for a monatomic gas.

Using the above equations, and converting density into an emissivity using XSPEC, as discussed in Sect. 2.3, we find that in the energy band 0.8–2 keV, where *Chandra* and XMM-Newton are most sensitive, for an $\mathcal{M} = 4$ shock, the X-ray emissivity contrast between shocked and unshocked gas is a factor of 3 higher if the ambient gas is at a galaxy temperature of ~ 0.3 keV than if the external medium has a cluster temperature of ~ 4 keV.

Complications apply in reality, and in practice these are difficult to treat even with data from observatories as powerful as *Chandra* and XMM-Newton. Firstly, there is observational evidence that in supernova remnants the post-shock electrons are cooler than the ions [66, 106]. Secondly, the simple Rankine-Hugoniot equations do not take into account the fact that the bow

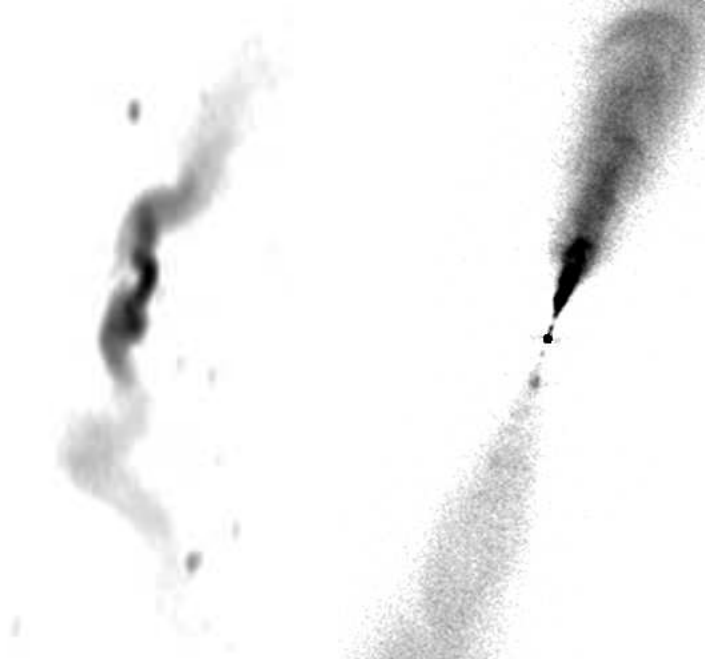


Fig. 8. Radio images of an example low-power FRI source, the radio galaxy 3C 31. The left image shows the large-scale structure. The map [80] has a resolution of 29×52 arcsec and is from a 608 MHz observations using the Westerbork Synthesis Radio Telescope. The angular length is about 40 arcmin which, at the galaxy's redshift of $z = 0.0169$, corresponds to about 830 kpc ($H_o = 70 \text{ km s}^{-1} \text{ Mpc}^{-1}$). The right image shows an 8.4-GHz VLA map of the inner ~ 18 kpc where the jets are relatively straight. The resolution is 0.25 arcsec, and the data are from [78]

shock around a lobe is oblique away from its head, with a consequent change in the jump conditions and the emissivity contrast [135]. However, in Sect. 6.5, we describe how the above equations can also be applied to an overpressured lobe in the inner structure of the low-power radio galaxy Cen A. The closer such a structure is to a spherical expansion, the more normal the shock will be everywhere and the better the applicability of the above equations.

5.2 Low-power FRI jets

The appearance of low-power jets, in FRI radio galaxies, is quite different from that of high-power jets: compare Fig. 7 with Fig. 8. Whereas the high-power jets in FRII radio sources are generally weak features within the well-defined, and much brighter radio lobes, low-power jets are usually of high contrast against the inner radio structures. Low-power jets are usually brightest near the active galactic nucleus, and then fade gradually in brightness at

larger distances from the core, although this pattern is often interrupted by patterns of bright knots in all wavebands. FRI jets show a range of morphologies, from almost straight and symmetrical two-sided jets to the bent “head-tail” sources that are characteristic of low-power extended radio sources in clusters.

While it is believed that the same basic mechanism is responsible for the generation of low-power and high-power jets, it appears that low-power jets dissipate much of their energy without developing a well-defined beam head. This is often taken to indicate that low-power jets are in good contact with the external medium in which they are embedded, so that they share momentum and energy with entrained material as they propagate. The strong velocity shear between a fast-moving (originally relativistic, based on VLBI observations of the cores of low-power radio sources [50]) jet flow and the almost stationary external medium must generate instabilities at the interface [10], and drive the flow into a turbulent state. The physics of the resulting flow is far from clear, although with simplifying assumptions [8] it has been shown that subsonic and transonic turbulent jet flows can reproduce the general trend of radio brightness and jet width for plausible confining atmospheres. More recently, model fits [57] using (41) and (45) to X-ray measurements of the thermal atmosphere of 3C 31, coupled with results from high-dynamic range radio mapping [78] (Fig. 8), have led to a self-consistent model of the flow.

The kinematic model of 3C 31 [79] involves three distinct regions in the jet: an inner ~ 1 kpc long section of narrow jet where the flow is fast (relativistic) and the opening angle of the jet is small, a flaring region of ~ 2 kpc during which the jet broadens rapidly and brightens in the radio, and an outer region in which the jet expands steadily with a smaller opening angle than in the flaring region. Here the jet decelerates steadily from a moderate Mach number as it picks up mass from the external medium or from the mass lost by stars embedded in the jet [73]. Buoyancy forces are important for much of the outer flow, and the jet becomes sensitive to local changes in the density of the intracluster medium, and hence is liable to deflect from straight-line motion.

While this model provides a good description of 3C 31, which displays a smoothly-varying radio brightness profile and so is amenable to simple fitting for flow speed, and is based simply on the basic conservation laws for mass, momentum, and energy [9], it represents only the overall deceleration of the jet from entrainment. This leaves unanswered important questions about the origins of the bright knots which appear in many jets, and which are interpreted as the sites of strong shocks (which are relativistic, based on proper motion studies), and about the detailed physics responsible for mass entrainment and the deceleration of the jet.

While the knots in jets are sites where intense acceleration of particles to highly relativistic energies can take place, it is clear from the diffuse X-ray

and other emission between the knots that there is continuing particle acceleration even in the inter-knot regions. The structures of the acceleration regions can only be studied in detail in the closest radio galaxies, such as Cen A [58] and M 87 [99]. A number of features of the knots have become apparent through detailed multiwavelength studies, of which the most important are the presence of high-speed motions (apparent speeds greater than the speed of light having been noted in M 87), and the distinct locations for the acceleration of particles radiating in different wavebands.

6 The interpretation of multiwavelength data in terms of physical parameters

6.1 Minimum energy and magnetic field strength

The evidence for magnetic fields in the jets and lobes of active galaxies (Sect. 6.6) confirms the synchrotron origin of the radio emission, which is therefore an inseparable function of the magnetic-field strength and electron spectrum. To progress further it is usual to assume that the source is radiating such that its combined energy in particles and magnetic field is a minimum [20]. In this situation the energy in the magnetic field is $\sim 3/4$ of the energy in the particles, and so this is similar to the condition in which the two are equal and the source is in “equipartition”.

We can calculate the minimum-energy magnetic field for a power-law spectrum using the equations in Sect. 2.1, and for more complicated spectra results can be obtained via numerical integration. The total energy in electrons

$$U_e = \kappa m_e c^2 \int_{\gamma_{\min}}^{\gamma_{\max}} \gamma \gamma^{-p} d\gamma = \kappa m_e c^2 \int_{\gamma_{\min}}^{\gamma_{\max}} \gamma^{-2\alpha} d\gamma \quad (52)$$

From (7), the synchrotron luminosity per unit frequency is

$$L_\nu \propto \kappa \nu^{-\alpha} B^{\alpha+1} \quad (53)$$

and we can eliminate κ from (52) and (53) to give (for $\alpha \neq 0.5$)

$$U_e \propto L_\nu \nu^\alpha B^{-(\alpha+1)} (\gamma_{\max}^{1-2\alpha} - \gamma_{\min}^{1-2\alpha}) (1 - 2\alpha)^{-1} \quad (54)$$

If K is the ratio of energy in heavy non-radiating particles to that in electrons, and η is the filling factor in the emission region of volume V , the energy density in particles can be written as

$$u_{\text{pcl}} = C_1 B^{-(\alpha+1)} \frac{(1+K)}{\eta V} L_\nu \nu^\alpha (\gamma_{\max}^{1-2\alpha} - \gamma_{\min}^{1-2\alpha}) (1 - 2\alpha)^{-1} \quad (55)$$

where the constant of proportionality, C_1 , is determined from synchrotron theory and can be expressed explicitly using the equations in Sect. 2.1. The energy density in the magnetic field can be written as

$$u_B = C_2 B^2 \quad (56)$$

where the value of the constant C_2 depends on the system of units. The value of B which minimizes the sum of the two energy densities, B_{me} , is then given by

$$B_{\text{me}} = \left[\frac{(\alpha + 1)C_1 (1 + K)}{2C_2} \frac{(1 + K)}{\eta V} L_\nu \nu^\alpha \frac{(\gamma_{\text{max}}^{1-2\alpha} - \gamma_{\text{min}}^{1-2\alpha})}{(1 - 2\alpha)} \right]^{1/(\alpha+3)} \quad (57)$$

Since luminosity density and flux density, S_ν , are related by

$$L_\nu = (1 + z)^{\alpha-1} S_\nu 4\pi D_L^2 \quad (58)$$

where D_L is the luminosity density, and the volume of a radio source can be specified [90] in terms of its angular component sizes, θ_x , θ_y and path length through the source, d , as

$$V = \theta_x \theta_y d D_L^2 / (1 + z)^4 \quad (59)$$

we find

$$B_{\text{me}} = \left[\frac{(\alpha + 1)C_1 (1 + K)}{2C_2} \frac{(1 + K)}{\eta \theta_x \theta_y d} 4\pi S_\nu \nu^\alpha (1 + z)^{3+\alpha} \frac{(\gamma_{\text{max}}^{1-2\alpha} - \gamma_{\text{min}}^{1-2\alpha})}{(1 - 2\alpha)} \right]^{1/(\alpha+3)} \quad (60)$$

At minimum energy, the total energy density is $u_{\text{me}} = u_B(\alpha + 3)/(\alpha + 1) = u_{\text{pcl}}(\alpha + 3)/2$. Any change in the ratio of u_B to u_{pcl} increases the total energy and pressure of the source. Thus if, as seen in the southwest radio lobe of Cen A (Sect. 6.5), the minimum pressure is below that of the external medium, expansion can immediately be inferred if lobes are to stay inflated for an appreciable time. Using minimum energy, the magnetic fields in radio sources are generally estimated at 1-10 nT (10-100 μ Gauss).

The dependence of B_{me} on the lower and upper cut-off energies of the electron spectrum are weak, and since α is expected to be ~ 0.6 from shock acceleration [1], or larger where energy losses have steepened the spectrum, it is the lower energy which has most effect. There is a stronger dependence of B_{me} on $(1 + K)$, the ratio of energy in all particles to that in radiating electrons, and η . It is usual to adopt unity for both of these factors, which gives a true minimum value for the energy and pressure $[(\gamma - 1)$ times the energy density, where in this context γ is the ratio of specific heats, which is $4/3$ for a relativistic gas]. Indirect arguments are then applied to estimate

if $(1 + K)$ should be larger than unity or η less than unity for a particular source.

In the case of SSC, L_ν must be converted into a spectral number of photons per unit volume, n_ν [i.e., $n(\nu_o)$ in the equations of Sect. 2.2]. For a uniform spherical source, of radius r , the average value for n_ν is given by

$$n_\nu = \frac{3 r L_\nu}{4 c h \nu} \quad (61)$$

It is instructive to consider the effects of relativistic beaming (Sect. 3). For the case of a spherical blob, (58) is now the equation for $L_\nu \delta^{(3+\alpha)}$, and the total synchrotron luminosity in the source frame is reduced by a factor of δ^4 , with u_B and κ , the normalization of the electron spectrum, both reduced by δ^2 . SSC in the source frame is reduced by a factor of δ^6 , and thus sources which are more beamed have lower SSC to synchrotron flux ratios. [The factors of δ^2 become $\delta^{2(2+\alpha)/(3+\alpha)}$ for the jet case where $\delta^{(2+\alpha)}$ should be used.]

The minimum-energy assumption can be tested by combining measurements of synchrotron and inverse-Compton emission from the same electron population. If the inverse Compton process is responsible for most of the higher-energy radiation that is measured, and the properties of the photon field are well known, the electron population is probed directly (Sect. 2.2). In combination with measurements of radio synchrotron emission from the same electrons, both the electron density and magnetic field strength can then be estimated, and the minimum-energy assumption can be tested. Since the application of this test requires that the volume and any bulk motion of the emitting plasma be known, the best locations for testing equipartition are the radio hotspots, which are relatively bright and compact, and are thought to arise from sub-relativistic flows at jet termination (but see [46]), and old radio lobes that should be in rough overall pressure balance with the external medium. There is no reason to expect dynamical structures to be at minimum energy.

Chandra has allowed such tests to be made on a significant number of lobes and hotspots, with results generally finding magnetic field strengths within a factor of a few of their minimum energy (equipartition) values for $(1 + K) = \eta = 1$ (e.g., [19, 56]). A study of ~ 40 hotspot X-ray detections concludes that the most luminous hotspots tend to be in good agreement with minimum-energy magnetic fields, whereas in less-luminous sources the interpretation is complicated by an additional synchrotron component of X-ray emission [59].

6.2 Jet composition

Much of the detailed physics of jets depends on what they contain. While it is clear from their polarized radiation that jets contain fast charged particles and magnetic fields, it is less clear whether these are primary energy-carrying

constituents of the jet or secondary. A number of different possibilities for the energy carriers have been suggested. The most popular are that the jets are primarily composed of electrons and positrons, or of electrons and protons, although electromagnetic (Poynting flux) jets [108] and proton-dominated jets [84, 104] have been discussed.

Since jets are presumed to obtain much of their energy from the infall of matter into a supermassive black hole, it is natural to suppose that electromagnetic radiation would carry much of the energy from the system on the smallest scales, since a plausible mechanism for the extraction of energy from the system is the twisting of magnetic field linked to the accretion disk. [82] describe the processes that might launch such a jet, but fast interactions with the plasma environment and efficient particle acceleration are expected quickly to load the field with matter. In the resulting magnetohydrodynamic flow much of the momentum would be carried by particles, although Poynting flux may carry a significant fraction of the total energy [5].

An electron-positron pair plasma is a natural consequence of the high energy density near the centres of active galaxies, and hence it might be expected that electrons and positrons would be an important, and perhaps dominant, component of the jet outflow. Acceleration of such a plasma by the strong radiation field near the active nucleus is certainly possible [93, 109], although radiation drag is an important limitation on the speeds to which the flow can be accelerated if only electron-positron pairs are present [121]. The importance of electron-positron pairs can be established by assuming that they are the major constituents of the flow, and then testing that the kinetic energy that they carry down the jet is comparable with the radiated power. While an electron-positron jet with arbitrary distribution of Lorentz factors, $N(\gamma)$, can satisfy this condition, an electron-proton jet should not extend to Lorentz factors $\gamma_{\min} < 100$, to avoid a high order of inefficiency and depolarization by Faraday rotation (Sect. 6.6). Another test, based on the assumption that the hotspots at jet termination in the FRII radio galaxy Cygnus A are reverse shocks in the jet fluid [72], suggests that the jet material is an electron-positron fluid at that point.

Further information supporting the interpretation of jets as electron-positron plasmas at their point of injection has been obtained by VLBI polarization studies [134]. Here the detection of circular polarization, interpreted as arising from mode conversion, strongly suggests that, on the pc scale, jets have low γ_{\min} (< 20) and hence are electron-positron plasmas (Sec. 6.6), although [110] find that other possibilities (notably that the jet is composed of electrons and protons) are not ruled out since other mechanisms exist for the generation of circular polarization.

There are also grounds for expecting high-power jets to contain a considerable fraction of their mass in protons. Protons outnumber electrons by 100 to 1 in Galactic cosmic rays at energies at which they leak out of the galaxy before significant energy loss [138]. Some jet acceleration mechanisms can

accelerate heavy components of the jets as much as, or more than, the lighter components, and, even if the jet is initially light, interactions with the external medium are expected to load it with protons (Sec. 5.2). However, there is little direct evidence for the proton contents of jets. Polarization studies do not find evidence of embedded thermal material, and protons are relatively inefficient radiators so the synchrotron emission of relativistic protons is probably not detectable (but see [2]). It does seem to be clear that jets are of low density relative to the external medium, on the basis of numerical simulations, since the structures of dense jets are unlike those observed, but there could still be appreciable mass in the flow.

Support for the presence of protons is also found in models for the broadband spectral energy distributions of emission from some sub-parsec scale quasar jets, where a significant proton contribution is required to boost the kinetic power sufficiently to match the total radiated power [126]. Some radio lobes in low-power radio galaxies, if assumed to be radiating at minimum energy (Sect. 6.1), would collapse because the X-ray-emitting medium has a higher pressure [32]. Although there are several ways of boosting the internal pressure in such a situation, magnetic dominance would make the sources unusual, electron dominance can be ruled out by constraints on inverse-Compton scattering of the CMB, and non-relativistic protons are disfavoured on grounds of Faraday rotation (Sect. 6.6), leaving a relativistic proton component most likely. In contrast, there are other cases where the radio lobes would be overpressured with respect to the ambient X-ray-emitting medium if a relativistic proton contribution were included [56]. Although this in itself is not a major difficulty, since there are open issues concerning lobe expansion (Sect. 6.5), these are lobes for which the magnetic field can be measured (Sect. 6.1) and the sources are close to minimum energy when only the radiating electrons are considered.

It has been known for some time that the minimum pressure in low-power jets (calculated assuming an electron-positron plasma) is typically below that of the external X-ray-emitting medium, e.g., [42, 71, 91, 140]. However, this cannot be used simply to infer that the jets are launched as an electron-proton plasma to give them the extra required pressure. Low-power jets are believed to slow down to sub-relativistic speeds via entrainment of thermal material (Sect. 5.2), and even the most detailed hydrodynamical modeling, such as that which has been applied to 3C 31 by [79], does not decide the issue of primary jet content.

On balance it appears that the dominant energy-carrying constituents of jets are electrons and positrons, but that relativistic protons may also be important, particularly in momentum transport. However, the situation remains unclear, and there are degeneracies between the measurement of jet speed and jet composition which render this conclusion tentative.

6.3 Jet speed

The resolved X-ray jets (excluding hotspots) that *Chandra* detects in powerful radio sources are mostly in quasars, e.g., [28, 87, 112, 113, 117, 118, 119, 120], with the bright radio sources Pictor A and Cygnus A [136, 137] being exceptions. The quasar X-ray jet emission is one-sided, on the same side as the brighter radio jet, implying that relativistic beaming is important. Two-sided X-ray emission, such as that in the quasar 3C 9 [40] most likely does not imply the presence of counter-jet emission, but rather the presence of the more isotropic lobe, hotspot, or cluster-related emission expected at some level in all sources and detected in many, e.g., [56, 145].

Currently there are several tens of quasar X-ray jet detections. They have mostly been found through targeted programs to observe bright, prominent, one-sided radio jets. In most cases there has been no pre-existing reported optical jet detection, but there has been reasonable success from follow-up work. The level of many such detections lies below an interpolation between the radio and X-ray spectra, suggesting that synchrotron emission from a single power-law distribution of electrons is not responsible for all the emission, e.g., [113, 117], although it has been pointed out that since high-energy electrons lose energy less efficiently via inverse Compton scattering in the Klein-Nishina regime, the electron spectrum should harden at high energies and in some cases may produce a synchrotron spectrum that can match observations [35].

In order to avoid the total energy in particles and magnetic field being orders of magnitude above its minimum value, as would arise from a simple SSC explanation, the most widely favored model for the X-ray emission in these cases is that the X-rays are produced by inverse Compton scattering of CMB photons by the electrons in a fast jet (Sect. 3) that sees boosted CMB radiation and emits beamed X-rays in the observer's frame [27, 127]. The model can produce sufficient X-rays with the jet at minimum energy, but only if the bulk motion is highly relativistic (bulk Lorentz factor, $\Gamma \approx 5 - 20$) and the jet at a small angle to the line of sight. Although such a speed and angle are supported on the small scale by VLBI measurements, at least for the source which has guided this work, PKS 0637-752 [83, 117], the jet must remain highly relativistic hundreds of kpc from the core (after projection is taken into account) for the X-rays to be produced by this mechanism. This conclusion, based on multiwavelength data, has been something of a surprise, since earlier statistical studies of the structures of powerful radio sources suggested that jet velocities average only about $0.7c$ at distances of tens of kpc from the core [54, 133].

A difficulty with the interpretation of the X-rays from radio jets as due to inverse-Compton scattering of CMB photons by a fast jet is that the observed gradients in X-ray surface brightness at the edge of the knots are sharp [128]. Since the X-rays are generated from low-energy electrons (as the CMB photons are boosted in the electron rest frame), the lifetimes of the

electrons are long and it is difficult to see how X-ray knots in high-power jets can have a steeper gradient (as in PKS 0637-752, [117]) than radio knots, which are produced by electrons of similar or higher energy. Although [128] suggest that the effects of strong clumping in the jets may resolve this issue, a fast jet and the proposed mechanism is then no longer required, since such clumping would increase the SSC yield for a slow jet at minimum energy [117].

6.4 Particle acceleration in jets

The electrons that emit synchrotron radiation in the radio, optical, and X-ray wavebands are all ultrarelativistic (with Lorentz factors $> 10^3$). The existence of large numbers of such relativistic electrons depends on their acceleration to high energies *locally* within the jet, or hot-spot, since their lifetimes against synchrotron losses (Sec. 2.1) are usually less than the minimum transport times from the active nuclei. (This may not be the case if proton synchrotron radiation is important [2].) Particle acceleration is generally discussed for the cases of a particle interacting with a distributed population of plasma waves or magnetohydrodynamic turbulence, or shock acceleration. Reviews of these processes may be found in [13, 36, 37] and elsewhere.

Resolved X-ray jets in active galaxies with *low* radio power are detected with *Chandra* in sources covering the whole range of orientation suggested by unified schemes, suggesting that beaming is less important than in their more powerful counterparts. The several tens of detected sources range from beamed jets in BL Lac objects [12, 101] to two-sided jets in radio galaxies [29, 58], with most X-ray jets corresponding to the brighter radio jet, e.g., [55, 57, 60, 61, 88, 144, 146]. Several of the observations have been targeted at sources already known to have optical jets, from ground-based work or HST. However, it's easier [144] to detect X-ray jets in modest *Chandra* exposures than to detect optical jets in HST snapshot surveys, because there is generally better contrast with galaxy emission in the X-ray band than in the optical.

Inverse Compton models for any reasonable photon field suggest an uncomfortably large departure from a minimum-energy magnetic field in most low-power X-ray jets, e.g., [55]. Synchrotron emission from a single electron population, usually with a broken power law, is the model of choice to fit the radio, optical, and X-ray flux densities and the relatively steep X-ray spectra, e.g., [16, 55]. X-ray synchrotron emission requires TeV-energy electrons which lose energy so fast that they must be accelerated *in situ*.

The above arguments, applied to the bright northeast jet of the nearest radio galaxy, Cen A, find in favor of X-ray synchrotron emission [74], and the proximity of Cen A allows its acceleration sites to be probed in the greatest possible detail. Unfortunately the dramatic dust lane spanning the galaxy masks any optical jet emission. Proper motion of order $0.5c$, observed both in the diffuse emission and some knots of Cen A's radio jet, is indicative of bulk motion rather than pattern speed [58]. Since Cen A has a strong jet

to counter-jet asymmetry, (23) then suggests that the jet is at a small angle to the line of sight. Since this contradicts the evidence based on parsec-scale properties, and other considerations, that the jet is at about 50 degrees to the line of sight, Cen A appears to be a case where intrinsic effects render (23) inapplicable. Some of the bright X-ray knots have only weak radio emission with no indication of proper motion, but with the radio emission brightening down the jet in the direction away from the nucleus. While the radio association confirms that these X-ray knots are indeed jet related, the emission profiles are not what are expected from a simple toy model where the electrons are accelerated and then advect down the jet, with the X-ray emitting electrons losing energy faster than the radio-emitting electrons. Instead, it is proposed [58] that there are obstacles in the jet (gas clouds or high-mass-loss stars). Both radio and X-ray-emitting electrons are accelerated in the standing shock of this obstacle, and a wake downstream causes further acceleration of the low-energy, radio-emitting, electrons. The resulting radio-X-ray offsets, averaged over several knots, could give the radio-X-ray offsets seen in more distant jets, e.g., [55].

The X-ray and radio emission in hot-spots are also offset in some cases [56], presumably also because of the different locations of acceleration of the particles at the different energies probed in these wavebands, if the emission is all synchrotron. However, it is expected that much of the X-ray emission should be of inverse-Compton origin, and then the offsets become harder to understand, although [46] have described a model in which decelerations of the jet plasma near a hot-spot can generate X-ray enhancements and small offsets.

Optical polarization might help us to learn more about the acceleration processes in low-power jets. In M 87 there is evidence for strong shock acceleration at the base of bright emitting regions, in compressed transverse magnetic fields [99]. A knot in the jet of M 87 has been observed to vary in the X-ray and optical on the timescale of months, consistent with shock acceleration, expansion, and energy losses [62, 100].

6.5 Pressure and confinement

It is interesting to compare the minimum pressure (Sect. 6.1) in radio lobes with that of the external X-ray-emitting environment. Over-pressure in the lobe would imply an expansion, which may be supersonic and should involve significant heating of the external gas. Under-pressure suggests either that the lobe is undergoing collapse (this should be rare given their prevalence) or that there is an additional component of pressure that may be in the form of relativistic protons. FRII sources are generally at high redshift where observations lack sufficient sensitivity and resolution to draw strong conclusions. However, notwithstanding the fact that there is no reason to expect dynamical structures to be at minimum energy, where tests are possible it tends

to be confirmed (Sect. 6.1), and it appears that with this assumption rough pressure balance prevails, e.g., [7, 33, 56].

The situation in low-power radio galaxies is more complicated, because the medium plays an important role in the deceleration of the jets, such that they share momentum and energy with entrained material. However, these sources have the advantage of being closer, and Sect. 5.2 describes how the pressure profile predicted by the mass-entrainment model for deceleration of the jet in 3C 31 gives an excellent match to observations. The outer radio structures of FRIs may sometimes be buoyant, e.g., [143], and in other cases show evidence of having done significant work on the gas in pushing it aside [15, 89], or responsibility for lifting gas in hot bubbles, e.g., [31], expected to result in eventual heating, e.g., [105]. Such heating would help to explain the weakness or absence of lines from gas cooling below 1 keV in the densest central regions of galaxy and cluster atmospheres, e.g., [102]. A statistical study shows that atmospheres containing radio sources tend to be hotter than those without [32].

One place where heating is definitely expected is from gas crossing the supersonically advancing bow shock of an expanding lobe (Sec. 5.1). It is possible to interpret X-ray cavities coincident with the inner parts of the radio lobes of Cygnus A as due to an emissivity contrast between bow-shock heated gas outside the lobes and the more easily detected ambient cluster medium [24], although the parameters of the shock are not effectively constrained by the data. More recent *Chandra* observations of Cygnus A find gas at the sides of the lobes to have $kT \sim 6$ keV, slightly hotter than the value of 5 keV from ambient medium at the same cluster radius, possibly indicating cooling after bow-shock heating, but again the data do not usefully constrain model parameters [122].

The first and best example of a shell of heated gas which can reasonably be attributed to supersonic expansion is not in an FR II radio source, but in Cen A (Fig. 9). High-quality *Chandra* and XMM-Newton data [74] provide the temperature and density constraints needed to test the model and measure the supersonic advance speed of the bow shock responsible for the heating. This source is an excellent example where much of the theory outlined earlier in this chapter can be applied.

Cen A is our nearest radio galaxy, at a distance of 3.4 Mpc [67] so that 1 arcsec corresponds to ~ 17 pc. The full extent of Cen A's radio emission covers several degrees on the sky [69]. Within this lies a sub-galaxy-sized double-lobed inner structure [21] with a predominantly one-sided jet to the northeast and a weak counter-jet to the southwest [58], embedded in a radio lobe with pressure 1.4×10^{-12} Pa or more, greater than the pressure in the ambient ISM ($\sim 1.8 \times 10^{-13}$ Pa; Table 1), and so which should be surrounded by a shock. Around this southwest lobe there is a shell of X-ray emitting gas which appears to have the geometry of the shocked ambient gas in Fig. 6 [75]. Although the capped lobe is around the weak counterjet, so it is not

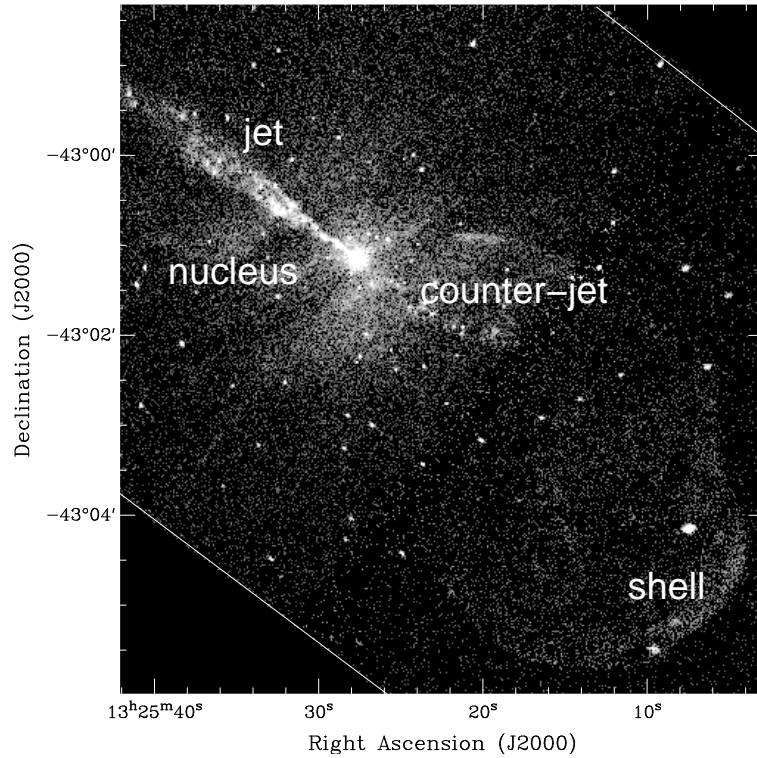


Fig. 9. 0.5–5 keV X-ray image of Cen A from a 50 ks *Chandra* exposure using the ACIS-S instrument. Pixel size is 1 arcsec. Data are exposure-corrected. Many point sources associated with Cen A’s host galaxy NGC 5128 are seen, together with a diffuse background of X-ray-emitting gas of $kT \approx 0.3$ keV, and labelled X-ray structures that are in whole or part related to radio structures (see the text and [38, 58, 74, 75] for more details)

evident that the lobe is being thrust forward supersonically with respect to the external interstellar medium (ISM) by the momentum flux of an active jet, the current high internal pressure in the radio lobe ensures its strong expansion.

The temperature, proton density and pressure of the ambient ISM and the X-ray shell, taken from [75] are given in Table 1. The ambient medium is measured to have $n_p \sim 1.7 \times 10^3 \text{ m}^{-3}$ and $kT = 0.29$ keV, whereas the shell is ten times hotter, at $kT = 2.9$ keV, and twelve times denser, with $n_p \sim 2 \times 10^4 \text{ m}^{-3}$. From (51) and (50), we see that temperature and density measurements for both the ambient medium and the shocked gas directly test shock heating, since only two of the four parameters are required to measure the Mach number, and the other two test the model.

Table 1. Physical parameters of the gas in various regions of Cen A

Structure	kT (keV)	n_p (m^{-3})	Pressure (Pa) [†]	0.4–2 keV relative emissivity, \mathcal{E}
ISM (measured)	0.29	1700	1.8×10^{-13} [‡]	1
Behind bow shock (inferred)	6.8	6530	2.1×10^{-11}	13
Shell (measured)	2.9	20000	2.1×10^{-11}	127

[†] 1 Pascal = 10 dyn cm^{-2}

[‡] incorrectly reported in Table 5 of [75]

ISM and Shell pressures are thermal only. Inferred pressure includes ram pressure of $\rho_1 v_{\text{adv}}^2 (\mathcal{M}^2 + 3)/4\mathcal{M}^2$

The minimum-energy pressure in the radio lobe is $\sim 1.4 \times 10^{-12}$ Pa.

The most straightforward application of the equations finds that the densities and temperatures are not self-consistent. The shell's density and temperature are wrong for gas directly in contact with the bow shock. However, we can find a Mach number consistent with shocking the gas to a temperature and density such that the combined thermal and ram pressure is in pressure equilibrium with the thermal pressure of the detected shell: $\mathcal{M} = 8.5$, $v_{\text{adv}} \approx 2400 \text{ km s}^{-1}$. The post-shock temperature is $kT_2 \sim 6.8 \text{ keV}$. The 6.8 keV gas flows back from the shock, into the X-ray-detected shell at 2.9 keV. The characteristics of this undetected hotter gas are given in Table 1. In this table we also quote estimates of the relative X-ray emissivity (per unit volume) of gas in the different structures over the 0.4–2 keV energy band, where the *Chandra* response peaks and is relatively flat. The gas directly behind the bow shock has a predicted emissivity that is an order of magnitude fainter than that in the shell, accounting for its non-detection in our measurements.

The radiative timescale for material in the shell is $\sim 2 \times 10^9$ yrs (Fig. 5), which is large compared with the lobe expansion time ($< 2.4 \times 10^6$ years), so the material in the shell behaves as an adiabatic gas [3]. The shell is overpressured compared with the minimum-energy pressure in the radio lobe (in magnetic field and radiating electrons) by a factor of ~ 10 . If we assume minimum energy in the lobe, despite it being a dynamical structure, and that the shell has reached equilibrium [but note that the sound-crossing time in the shell (thickness $\sim 0.3 \text{ kpc}$, $c_s \sim 9 \times 10^{-7} \text{ kpc yr}^{-1}$) is about 15 per cent of the maximum time we estimate it has taken the lobe to reach its current size], the shell's overpressure relative to the radio lobe could be balanced by the ram pressure from internal motions in the lobe for a moderate relativistic proton loading. Finally, the shell's kinetic energy is ~ 5 times its thermal energy, and exceeds the thermal energy of the ISM within 15 kpc of the centre of the galaxy. As the shell dissipates, most of the kinetic energy should ultimately be converted into heat and this will have a major effect on Cen A's ISM, providing distributed heating.

6.6 Magnetic field structures

Jets contain significant magnetic fields. The orientation of these fields is displayed by the linear polarization that they show in their radio synchrotron emission, and for many years detailed maps of the radio polarizations of jets have been used to infer the magnetic field geometries both on kpc scales, e.g., for NGC 6251 [98] and 3C 31 [43], and pc scales, e.g., for BL Lac objects [26].

The fractional linear polarization expected from an optically-thin synchrotron-emitting plasma is

$$\pi_L = \frac{\alpha + 1}{\alpha + \frac{5}{3}} \quad (62)$$

where α is the radio spectral index, and it is assumed that the frequency of observation satisfies $\gamma_{\min}^2 \nu_g \ll \nu \ll \gamma_{\max}^2 \nu_g$, as for (7). The electric field of the emitted radiation is perpendicular to the magnetic field within which the emitting electron population lies, so that an observation of the plane of polarization of the radio emission can be used to infer the geometry of the magnetic field within the radio jet.

In mapping the direction of the projected magnetic field, account has to be taken of the effect of Faraday rotation of the plane of polarization by mixed thermal material and fields within and around the radio jets. For a foreground plane slab of plasma, at a wavelength of λ , the Faraday rotation is an angle

$$\theta_F = \text{RM} \lambda^2 \quad (63)$$

where the rotation measure along path length L is

$$\text{RM} = \frac{1}{c} \int_0^L n_{e,\text{th}} r_e \nu_g \cos \psi dz \quad (64)$$

where $n_{e,\text{th}}$ is the thermal electron density, r_e is the classical electron radius, ν_g is the non-relativistic gyrofrequency, and ψ is the angle of the magnetic field to the line of sight. In SI units,

$$\text{RM} = 8100 \int_0^L n_{e,\text{th}} B_{\parallel} dz \quad \text{rad m}^{-2} \quad (65)$$

for a magnetic field with line-of-sight component B_{\parallel} (in Tesla), where $n_{e,\text{th}}$ is in m^{-3} and the thickness L is in pc. If the thermal material is mixed with the radio jet's plasma, an effect half this size is expected. If the magnetic field and thermal material have a complicated structure, different dependencies of θ_F on λ are possible. Faraday rotation is measured by multi-frequency radio mapping, and uncertainties in the intrinsic plane of polarization of the radio emission are minimized by working at high radio frequencies.

Since the presence of an appreciable density of thermal material around the jets is revealed in X-rays (Sect. 4), a significant Faraday rotation is possible if this medium contains a magnetic field, and some evidence for such Faraday rotation has been seen, e.g., in Hercules A [63], with the brighter, and presumably Lorentz-boosted, jet often showing a lower Faraday rotation than the opposite jet, as might be expected from simple geometrical considerations [45, 77].

A more important consequence of the significant linear polarizations measured for radio jets, however, is that those jets cannot contain large amounts of thermal material. If they did, then the change in θ_F between the front and back sides of the jets would lead to linear polarizations far less than the observed values, which are sometimes near the theoretical maximum given by (62). The limits on Faraday depolarization thus lead us to conclude that the X-rays from radio jets and lobes cannot come from thermal material mixed with the jets.

Polarization mapping also reveals that the magnetic fields in radio jets are relatively well ordered. In many jets of both high and low radio power the magnetic fields are longitudinal for the first few kpc of the length of the jet, then, in lower-power jets, the magnetic field becomes perpendicular to the jet axis at larger distances from the core, often after a significant change in the jet's width [17]. Variations on this pattern are seen where bright emission knots exist in the jet. These knots appear to be associated with strong shocks, which compress the magnetic field strongly into a transverse pattern at the upstream (core-side) of the knot, after which the magnetic field pattern becomes complicated. A particularly good example [99] is M 87, where the use of HST to map the optical polarization provides additional information, since the lifetimes of the electrons emitting optical synchrotron emission are far shorter than those of radio-emitting electrons. Significant differences between the polarization structures seen in the optical and radio in M 87 suggest that the sites of acceleration are different for different electron energies, with the strongest shocks, that provide acceleration to the highest energies, appearing in the most central parts of the jet.

In the central parts of radio sources, VLBI observations have been able to detect both linear and circular polarization. A distinct difference is seen in the polarizations of the pc-scale (VLBI) jets of BL Lac objects and radio galaxies or quasars. Generally, the magnetic field orientation in the cores of the highest-power sources is along the jet [26], but in lower-power sources, such as BL Lac objects, regions of significant transverse field are seen, and change on short timescales [44]. Again this is interpreted as the effect of shock structures moving along the jets, compressing the magnetic field as they pass, although helical patterns in the flow may affect the apparent field pattern, as may the effects of relativistic aberration. The lower linear polarizations often seen in pc-scale jets may be due to depolarization caused by the superposition of many small-scale structures, with different field orientations, within

the resolution of the observations, or perhaps to significant structure in the nuclear gas near the jet.

Circular polarization is generally undetectable in large-scale jets, but has been mapped in pc-scale jets using VLBI [64, 65], where it is interpreted as arising from mode conversion — the conversion of linear polarization to circular polarization by Faraday rotation in the jet plasma, although this is not certain [110]. If the X-ray emission from powerful jets on the large scale is interpreted as inverse-Compton scattering of CMB photons in a fast jet, then the population of relativistic electrons has to extend down to low energies (Lorentz factors $\gamma_{\min} = 10 - 20$, [27, 127]). On the other hand, the detection of significant polarization in VLBI jets implies that there should be few low-energy protons and electrons (which would cause excessive internal Faraday rotation), and hence that the jets should be composed of an electron-positron plasma. However, the presence of an electron-positron plasma in the VLBI jet does not necessarily imply its presence on the largest scales, where the jet may have become loaded with material gathered from the ambient medium or the radio lobe.

6.7 Cores: the inner jets

Radio jets extend into the cores of active galaxies, where they are faster and more compact. Special-relativistic effects then cause their brightness and variability time scales to be strong functions of jet orientation. As a result of synchrotron self-absorption, it is important to use VLBI techniques at high radio or mm frequencies to see close to the bases of jets.

The inner jets are difficult to distinguish at non-radio wavelengths because of their closeness to the central engine, which is bright at infrared to X-ray energies, and because of orientation-dependent absorption in the optical to soft-X-ray bands from gas and dust structures. These gas and dust structures are only sometimes detected, but their presence is often inferred so that models which unify various classes of active galaxy might work, e.g., [6]. They affect the central engine the most. Thus, the first problem in using multiwavelength data to gain additional insight into radio jets on small scales is to separate out the jet emission. For no waveband does telescope spatial resolution match that of radio VLBI, and so only the tool of spectral separation is usually available.

In the most core-dominated radio sources, such as bright variable BL Lac objects and quasars (often classed together as blazars), jet emission appears dominant at all energies, sometimes up to TeV. The multi-wavelength spectral energy distributions and variability time scales are used to probe the beaming parameters and the physical properties of the emitting regions, e.g., [48, 76, 125]. Correlated flares are sometimes measured across wavebands, giving support to the presence of a dominant spatial region of emission, e.g., [124, 131], but otherwise uncertainties of size scales, geometries, and parameters for the competing processes of energy loss and acceleration, often force

the adoption of oversimplified or poorly-constrained models for individual jets.

In the quasar population in general, there is good evidence that in the X-ray an inner jet dominates the emission from core-dominated quasars, but not lobe-dominated quasars, e.g., [18, 70, 141, 142, 148]. Radio galaxies are of particular interest, because here emission from the central engine is weak. In these sources a correlation of core soft-X-ray and radio emission, lost in lobe-dominated quasars, re-appears [22, 39, 52, 139], suggesting that jet-related X-ray emission is again dominant. In low-power radio galaxies, an optical core is often seen with HST, and is interpreted as synchrotron emission from a similar small-scale emitting region [23, 30, 53, 132]. However, at higher X-ray energies, a number of radio galaxies show clear evidence of a hard, highly absorbed continuum, sometimes accompanied by Fe-line emission, e.g., [51, 129]. Here the decreasing jet output is leading to the central engine becoming increasingly dominant. Both X-ray components can sometimes be distinguished in the same spectrum, e.g., [33, 38].

The richness of high-energy structure in larger-scale radio jets has been revealed because it is well resolved with HST and *Chandra*. Our knowledge of the inner jets is limited by the confusion of components that has now been lifted for the jets discussed earlier in this chapter.

7 Conclusion

The new results on radio jets which have resulted from complementary X-ray and optical observations have brought some surprises. Firstly, synchrotron X-ray jets are common in low-power sources, which implies that the intrinsic electron spectrum continues to TeV energies, and requires substantial *in situ* particle acceleration. Secondly, the detection of many quasar X-ray jets, most commonly interpreted as due to beamed CMB photons, would suggest that highly relativistic bulk flows exist far from the cores, contradicting earlier statistical studies of radio sources [54, 133]. Jet theory has had some pleasing successes, such as the agreement of the X-ray pressure profile with the prediction from a hydrodynamical model for 3C 31 [79].

There is still much observational work to be done. Firstly, there is considerable bias in the jets which have been observed in the X-ray, and we need observations of unbiased samples over broader luminosity and redshift ranges, together with observations of the X-ray-emitting medium through which the jets propagate. The measurements should elucidate the relative importance of synchrotron emission, inverse Compton scattering, and relativistic beaming, refine our knowledge of the source energetics, and improve constraints on jet composition and speed. Secondly, we need more deep X-ray observations (and refined theory) to understand jet-lobe/intercluster medium interactions. Finally, to study acceleration sites and processes, deeper and more detailed multiwavelength mapping, spectroscopy, and temporal monitoring

is required. In combination with multifrequency polarization measurements, such data could map the spatial distributions and follow the acceleration of the electrons responsible for the radiation in the radio to X-ray bands.

It should, however, be acknowledged that much basic physics of jets is still not well understood, e.g., the origin of the magnetic field, the method of jet production and collimation, and the effects of turbulence. Much theoretical work in these areas is necessary to relate measurements to the processes occurring in the fascinating jet flows that are observed.

References

1. A. Achterberg, Y.A. Gallant, J.G. Kirk, A.W. Guthmann: MNRAS **328**, 393 (2001)
2. F.A. Aharonian: MNRAS **322**, 215 (2002)
3. P. Alexander: MNRAS **335**, 610 (2002)
4. K. Arnaud, B. Dorman: XSPEC, An X-ray Spectral Fitting Package, version 11.3 <http://heasarc.gsfc.nasa.gov/docs/software/lheasoft/xanadu/xspec> (2003)
5. S. Appl, M. Camenzind: A&A **274**, 699 (1993)
6. P.D. Barthel: ApJ **336**, 606 (1989)
7. E. Belsole, D.M. Worrall, M.J. Hardcastle, M. Birkinshaw, C.R. Lawrence: MNRAS, in press (2004)
8. G.V. Bicknell: ApJ **286**, 68 (1984)
9. G.V. Bicknell: ApJ **422**, 542 (1994)
10. M. Birkinshaw: The stability of jets. In *Beams and Jets in Astrophysics*, ed by P.A. Hughes (Cambridge University Press), pp 278–341 (1991)
11. M. Birkinshaw, D.M. Worrall: ApJ **412**, 568 (1993)
12. M. Birkinshaw, D.M. Worrall, M.J. Hardcastle: MNRAS **335**, 142 (2002)
13. R.D. Blandford, D. Eichler: Phys. Rep. **154**, 1 (1987)
14. G.R. Blumenthal, R.J. Gould: Rev. Mod. Phys. **42**, 237 (1970)
15. H. Böhringer, W. Voges, A.C. Fabian, A.C. Edge, D.M. Neumann: MNRAS **264**, L25 (1993)
16. H. Böhringer, E. Belsole, J. Kennea et al: A&A **365**, L181 (2001)
17. A. Bridle, R.A. Perley: ARAA **22**, 319 (1984)
18. I.W.A. Browne, D.W. Murphy: MNRAS **226**, 601 (1987)
19. G. Brunetti, M. Bondi, A. Comastri, G. Setti: A&A **381**, 795 (2002)
20. G.R. Burbidge: ApJ **124**, 416 (1956)
21. J.O. Burns, E.D. Feigelson, E.J. Schreier: ApJ **273**, 128 (1983)
22. C.M. Canosa, D.M. Worrall, M.J. Hardcastle, M. Birkinshaw: MNRAS **310**, 30 (1999)
23. A. Capetti, A. Celotti, M. Chiaberge, H.R. de Ruiter, R. Fanti, R. Morganti, P. Parma: A&A **383**, 104 (2002)
24. C.L. Carilli, R.A. Perley, D.E. Harris: MNRAS **270**, 173 (1994)
25. A. Cavaliere, R. Fusco-Femiano: A&A **70**, 677 (1978)
26. T.V. Cawthorne, D.C. Gabuzda: MNRAS **278**, 861 (1996)
27. A. Celotti, G. Ghisellini, M. Chiaberge: MNRAS **321**, L1 (2001)
28. G. Chartas, D.M. Worrall, M. Birkinshaw et al: ApJ **542**, 655 (2000)

29. M. Chiaberge, R. Gilli, F.D. Macchetto, W.B. Sparks, A. Capetti: *ApJ* **582**, 645 (2003)
30. M. Chiaberge, A. Capetti, A. Celotti: *A&A* **349**, 77 (1999)
31. E. Churazov, M. Brüggen, C.R. Kaiser, H. Böhringer, W. Forman: *ApJ* **554**, 261 (2001)
32. J.H. Croston, M.J. Hardcastle, M. Birkinshaw, D.M. Worrall: *MNRAS* **346**, 1041 (2003)
33. J.H. Croston, M. Birkinshaw, M.J. Hardcastle, D.M. Worrall: *MNRAS* in press (2004)
34. C.D. Dermer: *ApJ* **446**, L63 (1995)
35. C.D. Dermer, A.M. Atoyan: *ApJ* **568**, L81 (2002)
36. L.O'C. Drury: *Rep. Prog. Phys.* **46**, 973 (1983)
37. J.A. Eilek, P.A. Hughes: Particle acceleration and magnetic field evolution. In *Beams and Jets in Astrophysics*, ed by P.A. Hughes (Cambridge University Press), pp 428–483 (1991)
38. D.A. Evans, R.P. Kraft, D.M. Worrall, M.J. Hardcastle, C. Jones, W.R. Forman, S.S. Murray: *ApJ*, in press (2004)
39. G. Fabbiano, L. Miller, G. Trinchieri, M. Longair, M. Elvis: *MNRAS* **277**, 115 (1984)
40. A.C. Fabian, A. Celotti, R.M. Johnstone: *MNRAS* **338**, L7 (2003)
41. B.L. Fanaroff, J.M. Riley: *MNRAS* **167**, 31P (1974)
42. L. Feretti, R. Fanti, P. Parma, S. Massaglia, E. Trussoni, W. Brinkmann: *A&A* **298**, 699 (1995)
43. E.B. Fomalont, A.H. Bridle, A.G. Willis, R.A. Perley: *ApJ* **237**, 418 (1980)
44. D.C. Gabuzda, T.V. Cawthorne: *MNRAS* **319**, 1056 (2000)
45. S.T. Garrington, J.P. Leahy, R.G. Conway, R.A. Laing: *Nature* **331**, 147 (1988)
46. M. Georganopoulos, D. Kazanas: *ApJ* **589**, L5 (2003)
47. G. Ghisellini, A. Celotti: *MNRAS* **327**, 739 (2001)
48. G. Ghisellini, A. Celotti, G. Fossati, L. Maraschi, A. Comastri: *MNRAS* **301**, 451 (1998)
49. V.L. Ginzburg, S.I. Syrovatski: *The origin of cosmic rays*. Pergamon Press, Oxford (1964)
50. G. Giovannini, W.D. Cotton, L. Feretti, L. Lara, T. Venturi: *ApJ* **552**, 508 (2001)
51. M. Gliozzi, R.M. Sambruna, W.N. Brandt: *A&A* **408**, 949 (2003)
52. M.J. Hardcastle, D.M. Worrall: *MNRAS* **309**, 969 (1999)
53. M.J. Hardcastle, D.M. Worrall: *MNRAS* **314**, 359 (2000)
54. M.J. Hardcastle, P. Alexander, G.G. Pooley, J.M. Riley: *MNRAS* **304**, 135 (1999)
55. M.J. Hardcastle, M. Birkinshaw, D.M. Worrall: *MNRAS* **326**, 1499 (2001)
56. M.J. Hardcastle, M. Birkinshaw, R.A. Cameron, D.E. Harris, L.W. Looney, D.M. Worrall: *ApJ* **581**, 948 (2002)
57. M.J. Hardcastle, D.M. Worrall, M. Birkinshaw, R.A. Laing, A.H. Bridle: *MNRAS* **334**, 182 (2002)
58. M.J. Hardcastle, D.M. Worrall, R.P. Kraft, W.R. Forman, C. Jones, S.S. Murray: *ApJ*, **593**, 169 (2003)
59. M.J. Hardcastle, D.E. Harris, D.M. Worrall, M. Birkinshaw: *ApJ*, in press (2004)
60. D.E. Harris, H. Krawczynski, G.B. Taylor: *ApJ* **578**, 60 (2002)

61. D.E. Harris, A. Finoguenov, A.H. Bridle, M.J. Hardcastle, R.A. Laing: ApJ **580**, 110 (2002)
62. D.E. Harris, J.A. Biretta, W. Junor, E.S. Perlman, W.B. Sparks, A.S. Wilson: ApJ **586**, L41 (2003)
63. N.A.B. Gizani, J.P. Leahy: MNRAS **342**, 399 (2003)
64. D.C. Homan, J.F.C. Wardle: AJ **118**, 1942 (1999)
65. D.C. Homan, J.F.C. Wardle: ApJ **602**, L13 (2004)
66. U. Hwang, A. Decourchelle, S.S. Holt, R. Petre: ApJ **581**, 1101 (2002)
67. F.P. Israel: A&A Rev **8**, 237 (1998)
68. D.L. Jones: ApJ **309**, L5 (1986)
69. N. Junkes, R.F. Haynes, J.I. Harnett, D.L. Jauncey: A&A **269**, 29 (1993)
70. A. Kembhavi: MNRAS **264**, 683 (1993)
71. N.E.B. Killeen, G.V. Bicknell, R.D. Ekers: ApJ **325**, 180 (1988)
72. M. Kino, F. Takahara: MNRAS **349**, 336 (2004)
73. A. Komissarov: MNRAS **269**, 394 (1994)
74. R.P. Kraft, W.R. Forman, C. Jones, S.S. Murray, M.J. Hardcastle, D.M. Worrall: ApJ **569**, 54 (2002)
75. R.P. Kraft, S.E. Vázquez, W.R. Forman, C. Jones, S.S. Murray, M.J. Hardcastle, D.M. Worrall, E. Churazov: ApJ **592**, 129 (2003)
76. H. Krawczynski, R. Sambruna, A. Kohnle et al.: ApJ **559**, 187 (2001)
77. R.A. Laing: Nature **331**, 149 (1988)
78. R.A. Laing, A.H. Bridle: MNRAS **336**, 328 (2002)
79. R.A. Laing, A.H. Bridle: MNRAS **336**, 1161 (2002)
80. J.P. Leahy: Atlas of radio sources. <http://www.jb.man.ac.uk/atlas/> (1998)
81. M.S. Longair: High Energy Astrophysics. 2nd ed. Cambridge University Press (1994)
82. R.V.E. Lovelace, H. Li, A.V. Koldoba, G.V. Ustyugova, M.M. Romanova: ApJ **572**, 445 (2002)
83. J.E.J. Lovell, S.J. Tingay, B.G. Piner et al: VSOP and ATCA observations of PKS 0637-752. In *Astrophysical Phenomena Revealed by Space VLBI*, ed by H. Hirabayashi, P.G. Edwards, D.W. Murphy (ISAS, Japan), pp 215–218 (2000)
84. K. Mannheim, P.L. Biermann: A&A **221**, 211 (1989)
85. A.P. Marscher: ApJ **264**, 296 (1983)
86. A.P. Marscher, F.E. Marshall, R.F. Mushotzky, W.A. Dent, T.J. Valonek, M.F. Hartman: ApJ **233**, 498 (1979)
87. H.L. Marshall, D.E. Harris, J.P. Grimes et al: ApJ **549**, L167 (2001)
88. H.L. Marshall, B.P. Miller, D.S. Davis, E.S. Perlman, M. Wise, C.R. Canizares, D.E. Harris: ApJ **564**, 683 (2002)
89. B.R. McNamara, M. Wise, P.E.J. Nulsen et al: ApJ **534**, L135 (2000)
90. G. Miley: ARAA **18**, 165 (1980)
91. R. Morganti, R. Fanti, I.M. Gioia, D.E. Harris, P. Parma, H. de Ruiter: A&A **189**, 11 (1988)
92. J.F. Navarro, C.S. Frenk, S.D.M. White: MNRAS **275**, 720 (1995)
93. S.L. O'Dell: ApJ **243** L147 (1981)
94. M.J.L. Orr, I.W.A. Browne: MNRAS **200**, 1067 (1982)
95. F.N. Owen, M.J. Ledlow: The FRI/II break and the bivariate luminosity function in Abell clusters of galaxies. In *The Physics of Active Galaxies*, ed by G.V. Bicknell, M.A. Dopita, P.J. Quinn (ASP Conf. Proc 54), pp 319–323 (1994)

96. A.G. Pacholczyk: Radio Astrophysics. W.H. Freeman and Co., San Francisco (1970)
97. T.J. Pearson, J.A. Zensus: Superluminal Radio Sources: Introduction. In *Superluminal Radio Sources*, ed by J.A. Zensus, T.J. Pearson (Cambridge University Press), pp 1–11 (1987)
98. R.A. Perley, A.H. Bridle, A.G. Willis: ApJS **54**, 291 (1984)
99. E.S. Perlman, J.A. Biretta, F. Zhou, W.B. Sparks, F.D. Macchetto: AJ **117**, 2185 (1999)
100. E.S. Perlman, D.E. Harris, J.A. Biretta, W.B. Sparks, F.D. Macchetto: ApJ **599**, L65 (2003)
101. J.E. Pesce, R.M. Sambruna, F. Tavecchio, L. Maraschi, C.C. Cheung, C.M. Urry, R. Scarpa: ApJ **556**, L79 (2001)
102. J.R. Peterson, F.B.S. Paerels, J.S. Kaastra et al: A&A **365**, L104 (2001)
103. E.S. Phinney: Central Radio Sources. In *Astrophysics of active galaxies and quasi-stellar object*, (University Science Books, Mill Valley CA), pp 453–496 (1985)
104. R.J. Protheroe, A.-C. Donea, A. Reimer: ApPh **19**, 599 (2003)
105. V. Quilis, R.G. Bower, M.L. Balogh: MNRAS **328**, 1091 (2001)
106. C.E. Rakowski, P. Ghavamian, J.P. Hughes: ApJ **590**, 846 (2003)
107. M.J. Rees: Nature **211**, 468 (1966)
108. M.J. Rees: Nature **229**, 312 and erratum 510 (1971)
109. N. Renaud, G. Henri: MNRAS **300**, 1047 (1998)
110. M. Ruszkowski, M.C. Begelman: ApJ **573**, 485 (2002)
111. G.R. Rybicki, A.P. Lightman: Radiative processes in astrophysics. Wiley, New York (1979)
112. R.M. Sambruna, C.M. Urry, F. Tavecchio, L. Maraschi, R. Scarpa, G. Chartas, T. Muxlow: ApJ **549**, L161 (2001)
113. R.M. Sambruna, L. Maraschi, F. Tavecchio, C.M. Urry, C.C. Cheung, G. Chartas, R. Scarpa, J.K. Gambill: ApJ **571**, 206 (2002)
114. C.L. Sarazin: Rev. Mod. Phys. **58**, 1 (1986)
115. P.A.G. Scheuer: Tests of beaming models. In *Superluminal Radio Sources*, ed by J.A. Zensus, T.J. Pearson, (Cambridge University Press), pp 1–113 (1987)
116. P.A.G. Scheuer, A.C.S. Readhead: Nature **277**, 182 (1979)
117. D.A. Schwartz, H.L. Marshall, J.E.J. Lovell et al: ApJ **540**, L69 (2000)
118. A. Siemiginowska, J. Bechtold, T.L. Aldcroft, M. Elvis, D.E. Harris, A. Dobrinska: ApJ **570**, 543 (2002)
119. A. Siemiginowska, R.K. Smith, T.L. Aldcroft, D.A. Schwartz, F. Paerels, A.O. Petric: ApJ **598**, L15 (2003)
120. A. Siemiginowska, C. Stanghellini, G. Brunetti et al: ApJ **595**, 643 (2003)
121. M. Sikora, H. Sol, M.C. Begelman, G.M. Madejski: MNRAS **280**, 781 (1996)
122. D.A. Smith, A.S. Wilson, K.A. Arnaud, Y. Terashima, A.J. Young: ApJ **565**, 195 (2002)
123. L. Spitzer: Physical Processes in the Interstellar Medium. Wiley, New York (1978)
124. T. Takahashi, J. Kataoka, G. Madejski et al: ApJ **542**, L105 (2000)
125. G. Tagliaferri, M. Ravasio, G. Ghisellini et al: A&A **400**, 477 (2003)
126. F. Tavecchio, L. Maraschi, G. Ghisellini et al: ApJ **543**, 535 (2000)
127. F. Tavecchio, L. Maraschi, R.M. Sambruna, C.M. Urry: ApJ **544**, L23 (2000)
128. F. Tavecchio, G. Ghisellini, A. Celotti: A&A **403**, 83 (2003)

129. S. Ueno, K. Koyama, M. Nishida, S. Yamauchi, M.J. Ward: *ApJ* **431**, L1 (1994)
130. C.M. Urry, P. Padovani: *PASP* **107**, 803 (1995)
131. C.M. Urry, A. Treves, L. Maraschi et al: *ApJ* **486**, 799 (1997)
132. G.A. Verdoes Kleijn, S.A. Baum, P.R. de Zeeuw, C.P. O'Dea: *AJ* **123**, 1334 (2002)
133. J.F.C. Wardle, S.E. Aaron: *MNRAS* **286**, 425 (1997)
134. J.F.C. Wardle, D.C. Homan, R. Ojha, D.H. Roberts: *Nature* **395**, 457 (1998)
135. A.G. Williams: Numerical Simulations of Radio Source Structure. In *Beams and Jets in Astrophysics*, ed by P.A. Hughes (Cambridge University Press), pp 342–378 (1991)
136. A.S. Wilson, A.J. Young, P.L. Shopbell: *ApJ* **547**, 740 (2001)
137. A.S. Wilson, A.J. Young, P.L. Shopbell: Chandra X-ray Observations of Cygnus A and Pictor A. In: *Particles and Fields in Radio Galaxies*, ASP Conf. Ser. Vol. 250, ed by R.A. Laing, K.M. Blundell (ASP, San Francisco), pp 213–223 (2001)
138. A.W. Wolfendale: Introductory cosmic rays. In: *Origin of Cosmic Rays*, Nato Advanced Study Institute Series, ed by J.L. Osborne, A.W. Wolfendale (Reidel, Dordrecht), pp 1–12 (1975)
139. D.M. Worrall, M. Birkinshaw: *ApJ* **427**, 134 (1994)
140. D.M. Worrall, M. Birkinshaw: *ApJ* **530**, 719 (2000)
141. D.M. Worrall, P. Giommi, H. Tananbaum, G. Zamorani: *ApJ* **313**, 596 (1987)
142. D.M. Worrall, C.R. Lawrence, T.J. Pearson, A.C.S. Readhead: *ApJ* **420**, L17 (1994)
143. D.M. Worrall, M. Birkinshaw, R.A. Cameron: *ApJ* **449**, 93 (1995)
144. D.M. Worrall, M. Birkinshaw, M.J. Hardcastle: *MNRAS* **326**, L7 (2001)
145. D.M. Worrall, M. Birkinshaw, M.J. Hardcastle, C.R. Lawrence: *MNRAS* **326**, 1127 (2001)
146. D.M. Worrall, M. Birkinshaw, M.J. Hardcastle: *MNRAS* **343**, L73 (2003)
147. D.M. Worrall, M.J. Hardcastle, T.J. Pearson, A.C.S. Readhead: *MNRAS* **347**, 632 (2004)
148. G. Zamorani: X-ray properties of extragalactic compact objects. In: *VLBI and compact radio sources*, IAU Symp. 110 ed by R. Fanti, K. Kellermann, G. Setti (Reidel, Dordrecht), pp 85–94 (1984)